Hydrostatic and [001] Uniaxial Pressure on Anatase TiO$_2$ by Periodic B3LYP-D* Calculations

Anderson R. Albuquerque,[†,§] Jefferson Maul,[†,§] Elson Longo,[‡] Iêda M. G. dos Santos,[†] and Julio R. Sambrano*,[§]

[†]Laboratório de Combustíveis e Materiais, Departamento de Química, CCEN, Universidade Federal da Paraíba, Campus I, CEP 58059 - 900, João Pessoa, PB, Brazil

[‡]LIEC, INCTMN-UNESP, São Paulo State University, CEP 14801-907, Araraquara, SP, Brazil

[§]Grupo de Modelagem e Simulação Molecular, INCTMN-UNESP, São Paulo State University, CEP 17033-360, Bauru, SP, Brazil

S *Supporting Information*

ABSTRACT: The effect of high hydrostatic and [001] uniaxial pressures on TiO$_2$ anatase was studied under the framework of periodic calculations with the inclusion of DFT-D2 dispersion potential adjusted for this system (B3LYP-D*). The role of dispersion in distorted unit cells was evaluated in terms of lattice parameters, elastic constants, equation of state, vibrational properties, and electronic properties (band structure and density of states). A more reliable description at high pressures was achieved because the B3LYP-D* presented an improvement in all properties for undistorted bulk over conventional B3LYP and B3LYP-D. From density of states analysis, we observed that the contribution of crystalline orbitals to the edge of valence and conduction bands changed within applied pressure. The studied distortions can give some insight into behavior of electronic and structural properties due to local stress in anatase bulk from doping, defects, and physical tensions in nanometric forms.
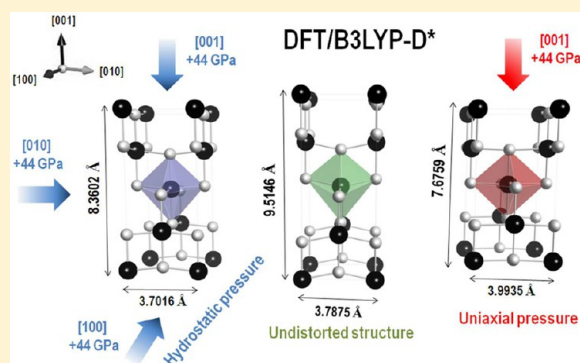
1. INTRODUCTION

Titanium dioxide (TiO$_2$) is a versatile wide-gap semiconductor of scientific and technological importance, with potential applications as hydrogen production from water splitting,[1] dye-sensitized solar cell,[2] microbiological agent,[3] photocatalyst,[4] catalytic support,[5] and others.

In the nature, TiO$_2$ has three common polymorphs: rutile, anatase, and brookite.[6] The anatase phase has received much attention lately due to its superior photocatalytic properties along with advances in crystal synthesis (morphology control with exposure of high reactive facets[7]) that emerged by computational and experimental studies.[8]

Predictions of anatase behavior under variable conditions of solvent, atmosphere, temperature, and pressure can guide its technological application. Some studies explored the pressure effects on structural, thermochemical, and electronic structure of TiO$_2$ polymorphs[9−16] and led to the identification of new types of physical and chemical behavior of interesting materials.

External stress can induce elastic strain and perturb the atomic bonding environment in bulk and surface structures. This effect are almost inevitable in nanostructures, thin films, and quantum dots fabrication.[17] Recently, it was observed that an application of external pressure increases aluminum and chromium solubility into TiO$_2$ within the formation of new orthorhombic TiO$_2$ polymorph with CaCl$_2$ structure.[12,14]

By means of computational calculations, high-pressure effects on selected directions can be simulated to provide several chemical and physical properties of solids. Beltrán et al.[18] studied the pressure-induced phase transition of TiO$_2$ polymorphs (anatase, rutile, and brookite) by periodic B3LYP computations. A valuable study conducted by Calatayud et al.[9] explored the chemical bonding and electronic structure of anatase under pressure up to 16 GPa by B3LYP and AIM (atoms in molecules) formalism. In a recent study, Mahmood et al.[15] investigated the effect of hydrostatic pressure (0−70 GPa) on the electronic, elastic constants, and optical properties of rutile TiO$_2$ within the DFT/PBE method.

High external pressure can also influence the chemical potential of point defects, as reported by Yoo et al.,[16] who used LDA+U and HSE hybrid functional to evaluate the oxygen vacancy chain formation in TiO$_2$ rutile under external strain and proposed its potential application in resistive random access memory.

Thulin and coworkers[19] studied electronic band structure of anatase over a range of biaxial strain by DFT/GGA and quasiparticle theory calculations within the GW approximation
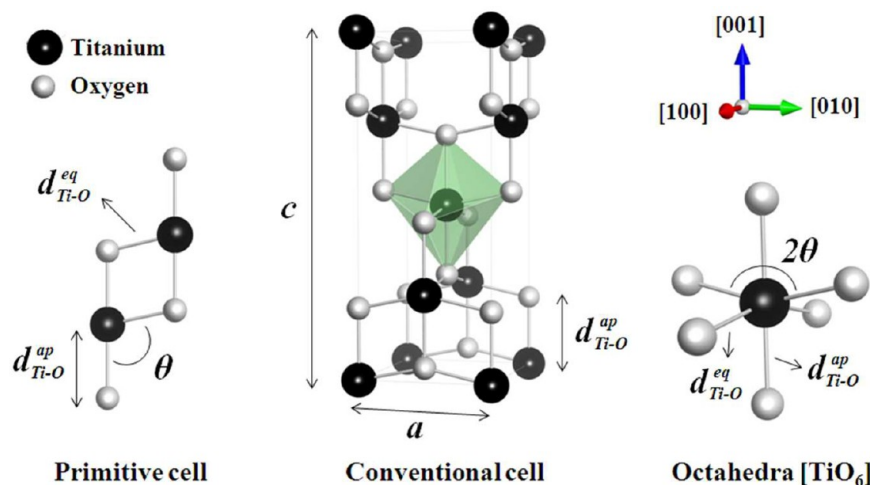
Figure 1. Representation of primitive and conventional TiO$_2$ anatase unit cell. The central [TiO$_6$] octahedra is in green.

to understand how pressure induced the narrowing on band gap and its effect on photoanode and photoelectrochemical properties. Similarly, Yin et al.[20] observed that the higher variations in band gap of anatase occur along the soft [001] crystal direction.

For better accuracy in periodic models simulations, weak interaction as dispersive energies can be taken into account. Conventional DFT methods require the inclusion of semi-empirical terms to describe these phenomena.[21−23] DFT augmented with an empirical dispersion term to pure Khon−Sham DFT energy (DFT-D) has demonstrated high accuracy in many different applications,[24,25] leading to a closer agreement with experimental data.

The general form of total energy in the DFT-D method is given by[26] $E_{DFT-D} = E_{KS-DFT} + E_{disp}$ where E_{KS-DFT} is the usual self-consistent Kohn−Sham energy from the arbitrary density functional and E_{disp} is a semiempirical dispersion term. CRYSTAL09 package[27,28] adopts the DFT-D2[26] adapted to periodic systems, as shown by eq 1

$$E_{disp} = -s_6 \sum_{i=l}^{N_{at}-1} \sum_{j=i+1}^{N_{at}} \sum_{\mathbf{g}} \frac{c_6^{ij}}{R_{ij,\mathbf{g}}^6} f_{dmp}(R_{ij,\mathbf{g}}) \tag{1}$$

where the summation is over all atom pairs and $\mathbf{g}$ lattice vectors with the exclusion of the $i = j$ contribution for $\mathbf{g} = 0$, s_6 is a scaling factor that depends only on the functional used (1.05 for B3LYP), c_6^{ij} is the dispersion coefficient for the atom pair ij computed by using a geometric mean, and $R_{ij,\mathbf{g}}$ is the interatomic distance between atoms i in the reference cell and j in the neighboring cells at distance $\|\mathbf{g}\|$. The damping function (f_{dmp}) (eq 2) is used to avoid near-singularities for small $R_{ij,\mathbf{g}}$ distances and is given by eq 2.

$$f_{dmp}(R_{ij,\mathbf{g}}) = \frac{1}{1 + e^{-d(R_{ij,\mathbf{g}}/R_{vdW}-1)}} \tag{2}$$

where $d = 20$ is the constant that determines the steepness of the damping function and R_{vdW} is the sum of van der Waals (vdW) atomic radii for atom pair ij.

Dispersion interactions are ubiquitous in nature as a result of dynamical correlations between fluctuating charge distributions[26,29] and then can be taken into account for an better accuracy on periodic models simulations. Recently, we[30] reported an augmented on TiO$_2$ anatase structure description

by periodic B3LYP-D* calculations using optimized titanium and oxygen cutoff radii in eq 2, with better results when compared with conventional B3LYP and B3LYP-D for undistorted anatase bulk.

In the present study, the behavior of TiO$_2$ anatase under high hydrostatic and [001] uniaxial pressures was investigated using periodic DFT calculations. The role of dispersion potential with DFT/B3LYP-D and DFT/B3LYP-D*[30] was evaluated and discussed in terms of lattice parameters, elastic constants, equation of state (EOS), normal vibrational modes, and electronic properties (band structure and density of states). The characteristics of [TiO$_6$] octahedra deformations induced by pressure were discussed based in Ti−O chemical bonding.

2. THEORETICAL CALCULATIONS AND MODELS SYSTEM

2.1. Anatase Structural Description. Anatase structure was modeled with a conventional unit cell composed of four units of TiO$_2$ in the periodic 3D structure $[(TiO_2)_4]_n$ (Figure 1).

TiO$_2$ anatase has a tetragonal structure belonging to the $I4_1/amd$ space group and defined by two lattice parameters (a and c) and one internal coordinate u ($u = d^{ap}_{Ti-O}/c$, where d^{ap}_{Ti-O} is the apical Ti−O bond length). This structure can be described as a stacked edge sharing octahedra of formal Ti^{4+} cation coordinated by six O^{2-} anions. These octahedra centered on Ti atom are distorted and have different bond lengths between apical (d^{ap}_{Ti-O}) and equatorial (d^{ap}_{Ti-O}) Ti−O bonds that form an angle of 180° (O$_{ap}$−Ti−O$_{ap}$) and $2\theta \approx 156°$ of (O$_{eq}$−Ti−O$_{eq}$). The internal parameter u determines the degree of shift on Ti−O apical bonds and leads to a local symmetry changing from $D_{2d} \rightarrow D_{4d}$ of [TiO$_6$] octahedra in the extreme case when $u = 0.250$. The local symmetry (C_{2v}) of oxygen remains under this condition.

2.2. Computational Details. Structural, vibrational, and electronic properties of undistorted (default structure at zero external pressure) TiO$_2$ anatase bulk, as well as the distorted systems, were investigated by means of periodic first-principles calculations in the framework of density functional theory (DFT) with the B3LYP hybrid functional[31,32] using the CRYSTAL 09 package.[27,28] CRYSTAL 09 uses Gaussian-type basis set to represent crystalline orbitals as a linear combination
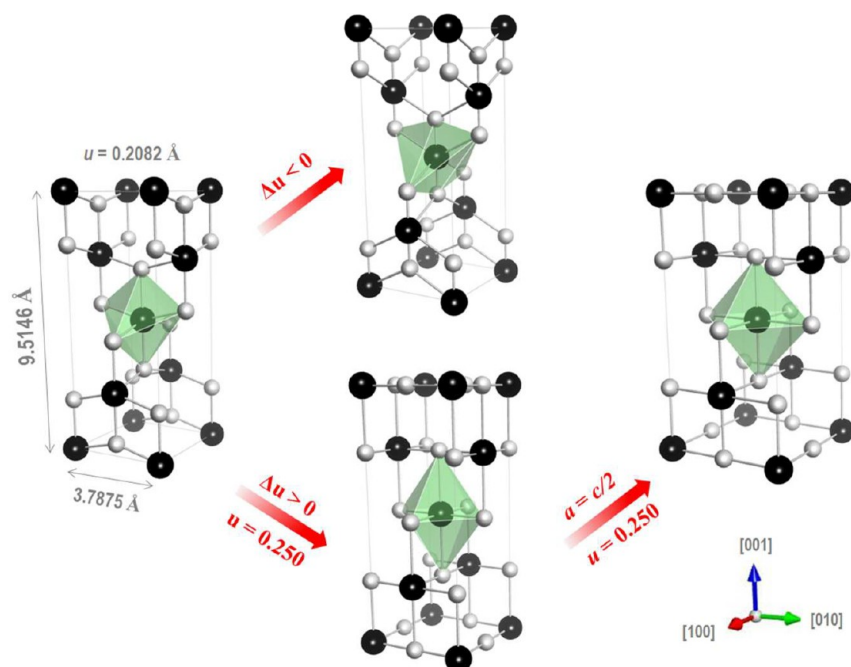
Figure 2. Idealized anatase unit cell with variable lattice and internal parameters to access central octahedra $D_{2d} \rightarrow D_{4d} \rightarrow O_h$ symmetry. The central octahedra of titanium are shown in green.

of Bloch functions defined in terms of local functions (atomic orbitals).

The oxygen and titanium centers were described by 6-31G* and 6-21(d-31)G all-electron basis set, respectively. The level of calculation accuracy for the Coulomb and exchange series was controlled by five thresholds set to (10^{-8}, 10^{-8}, 10^{-8}, 10^{-8}, 10^{-18}). The shrinking factor (Pack−Monkhorst and Gilat net) was set to 6, corresponding to 40 independent k points in the irreducible part of the Brillouin zone integration. A very large grid with 99 radial points and 974 angular points was adopted. The convergence threshold was set to 10^{-7}, 10^{-10}, and 10^{-8} Ha for SCF energy calculation on optimization, vibrational frequencies, and elastic constants, respectively.

Calculations were done with the inclusion of the dispersion potential to evaluate the relevance of dispersive energy in the high-pressure environment, as reported in ref 30.

Elastic constants were evaluated numerically from analytical gradients[33] and analyzed to determine the soft directions in bulk and predict its behavior under pressure. The elastic constants are second derivatives of the energy density with respect to strain components and provide important information on mechanical response to the external forces and its structural stability. Elastic constants changing within pressure were also determined.

The EOS was obtained to determine the relationship between energy, volume, and pressure starting from the undistorted structure. All structural parameters were full-optimized at fixed volumes (V) in the range $0.80 < V/V_0 < 1.20$ with increment of $0.01V_0$, where V_0 is the equilibrium unit cell volume under isothermal conditions ($T = 298$ K). The values of zero-pressure bulk modulus (B_0) and its pressure derivative (B_0') were generated by a fitting procedure within $E(V)$ third-order Birch−Murnaghan EOS.[34]

Hydrostatic and [001] uniaxial pressure were determined by applying fixed pressure ($0.0 < P/GPa < 45$) on unit cells by means of strain tensors **H** (eq 3) and **U** (eq 4), respectively, acting upon the **A** matrix that contains Cartesian components of the three elementary lattice vectors of the unstrained crystallographic unit cell to build the unit cells **A′** and **A″**.

$$\mathbf{A'} = \mathbf{A} \cdot \mathbf{H} = \begin{bmatrix} a & 0 & 0 \\ 0 & a & 0 \\ 0 & 0 & c \end{bmatrix} \cdot \begin{bmatrix} 1+\delta & 0 & 0 \\ 0 & 1+\delta & 0 \\ 0 & 0 & 1+\delta \end{bmatrix} = \begin{bmatrix} (1+\delta) \cdot a & 0 & 0 \\ 0 & (1+\delta) \cdot a & 0 \\ 0 & 0 & (1+\delta) \cdot c \end{bmatrix} \tag{3}$$

$$\mathbf{A''} = \mathbf{A} \cdot \mathbf{U} = \begin{bmatrix} a & 0 & 0 \\ 0 & a & 0 \\ 0 & 0 & c \end{bmatrix} \cdot \begin{bmatrix} 1 & 0 & 0 \\ 0 & 1 & 0 \\ 0 & 0 & 1+\delta \end{bmatrix} = \begin{bmatrix} a & 0 & 0 \\ 0 & a & 0 \\ 0 & 0 & (1+\delta) \cdot c \end{bmatrix} \tag{4}$$

Distorted structures were obtained by minimizing the total energy in relation to lattice parameters and atomic coordinates after each strain deformation.

The infrared and Raman shifts within pressure were also studied. The vibrational frequencies at the Γ point were computed within the harmonic approximation by diagonalizing the mass-weighted Hessian matrix. Details of the computational vibrational frequencies scheme can be found in refs 35 and 36.

Electronic band structures were obtained at the appropriate high-symmetry path in the first Brillouin zone,[37] and the density of states (DOS) were calculated according to the Fourier−Legendre technique, with polynomial degree equal to 10.

The graphical manipulations were carried out with MOLDRAW[38] and VESTA[39] for Microsoft Windows. The XCrySDen software for Linux was used to build electrostatic potential and charge-density maps.[40]

2.3. Model System for Octahedra Distortion. To evaluate the electronic structure with octahedra $[TiO_6]$ distortion, a series of auxiliary single-point calculations were performed, allowing a variation of the internal parameter u in the range of 0.208 (standard undistorted cell) $< u < 0.250$ from default unit cell at B3LYP-D* level, as shown in Figure 2.

The u parameter controls the degree of squeezing of $[TiO_6]$, and its variation enabled access to the local symmetry D_{2d} ($u < 0.250$) $\rightarrow D_{4d}$ ($u = 0.250$). The c/a ratio determines the polyhedral elongation, and an additional modification to $c/a = 2$ enabled access to $D_{4d} \rightarrow O_h$ local symmetry on $[TiO_6]$ octahedra. Their electronic structures were explored by projected density of states (PDOS).

These idealized periodic models can be useful to understand point defects and local unit cell deformations in metastable phases of anatase and structural motifs close to surfaces and interfaces, as a consequence of uncompleted coordination. Over the past decade, our research group has explored the effect of symmetry breaking on the introduction of intermediate electronic levels in the forbidden band gap and associated it with the photoluminescence phenomena,[41−44] which is linked to order−disorder effects due to the interaction between ordered (o) and distorted (d) clusters ($[TiO_6]_o$−$[TiO_6]_d$), with a global effect of decreasing the band gap.

3. RESULTS AND DISCUSSION

3.1. Structural Properties. The calculated cell parameters for undistorted TiO_2 bulk structure at B3LYP, B3LYP-D, and B3LYP-D* levels, as previously reported,[30] as well as recent theoretical calculations (with B3LYP and HSE06) and experimental values from single crystal are shown in Table 1. Published lattice parameters using B3LYP and the recent hybrid functional HSE06[45] are still far from experimental values. For the c parameter (z direction), the present B3LYP and B3LYP-D calculations overestimate this value by ~2%, as compared with experimental data. B3LYP-D* [30] are in good agreement with experimental data from anatase single crystal,[46] which makes it more reliable to study of distorted unit cell.

The hydrostatic pressure is isotropic and therefore acts equally in all directions, exercising a significant effect on soft directions. Uniaxial pressure acts in only one direction on the unit cell. The elastic constant (C_{ij}) calculations provide reliable information about those and are composed of the second derivatives of the energy density with respect to strain components (eq 5).

Table 1. Theoretical and Experimental Lattice Parameters a, c, u, c/a, and Conventional Unit Cell Volume (V_0) for Undistorted TiO_2 Anatase

| method | parameters/Å | | | c/a | $V_0/Å^3$ |
	$a = b$	c	u		
B3LYP-D*[a]	3.7875	9.5146	0.2082	2.512	136.5
B3LYP-D[a]	3.7698	9.7192	0.2057	2.578	138.1
B3LYP[a]	3.7972	9.7069	0.2055	2.556	140.0
B3LYP[9]	3.7723	9.9285	0.2028	2.632	141.3
B3LYP[55]	3.8117	9.7136		2.548	141.1
B3LYP[62]	3.7923	9.8240	0.2033	2.590	141.3
HSE06[45]	3.755	9.561	0.207	2.546	134.8
HSE06[49]	3.766	9.609		2.551	136.3
exp[46]	3.7842	9.5146	0.2081	2.514	136.3
exp[47]	3.78512	9.51185		2.513	136.3

[a]This work and ref 30.

$$C_{ij} = \frac{1}{V} \frac{\partial^2 E}{\partial \varepsilon_i \partial \varepsilon_j} \tag{5}$$

In the anatase tetragonal system, the six constants independent of strain are ($C_{11} = C_{22}$), C_{12}, ($C_{13} = C_{23}$), C_{33}, ($C_{44} = C_{55}$), and C_{66}. Mechanically, C_{11} and C_{33} corresponds to longitudinal distortion in $[100]$ and $[001]$ directions, respectively. C_{12} and C_{13} are scissors mode in $[110]$ and $[101]$ directions, respectively. C_{44} and C_{66} are elastic moduli for the twisting shear strains ε_{13} and ε_{12}, and their related stresses.

The calculated C_{ij} values for undistorted bulk by B3LYP, B3LYP-D, and B3LYP-D* were in accordance with other reported theoretical results, with an increasing order $C_{11} > C_{33} > C_{12} > C_{13} > C_{66} > C_{44}$, as reported in ref 30. For the best of our knowledge, experimental C_{ij} values for anatase single crystal were not found in literature. A reliable description of elastic constants allows us to calculate some related properties, such as acoustic wave speeds in different directions, load deflection, internal strain, and thermoelastic stress; it also helps to analyze the red/blue shift of vibrational frequencies within pressure.

3.2. Equation of State. The relative DFT ground-state equilibrium energies as a function of volume and the isothermal pressure−volume diagram are shown in Figure 3a,b, respectively, calculated at the B3LYP, B3LYP-D, and B3LYP-D* levels. The role of the dispersion potential is to decrease the total energy, mainly for compressed structures (Figure 3c), because the interatomic distance ($R_{ij,g}$) between atoms i in the reference cell and j in the neighboring cells at distance $\|g\|$ is in the denominator in eq 2. The dispersion energies as a function of volume are shown in Figure 3c. The small B3LYP-D* dispersion energy in relation to B3LYP-D is a consequence of $R_{vdW\ DFT-D*} < R_{vdW\ DFT-D}$.

The fitted EOS (E,V) provided the equilibrium geometry V_0 and bulk modulus B_0, displayed in Table 2. The bulk modulus is defined as the ratio of the infinitesimal pressure increase to the resulting relative decrease in the volume $B_0 = -V(\partial P/\partial V) = V(\partial^2 E/\partial V^2)$, and it measures the resistance to uniform compression. The highest value of B_0 by B3LYP-D* is due to the dispersion inclusion and a consequence of cell contraction, as compared with the conventional B3LYP method.

Experimental data from volume−pressure at room temperature for anatase bulk vary between 179 $\pm$ 2 GPa (single crystals) and 190 $\pm$ 10 GPa (polycrystalline system).[47] Recently, it was observed that bulk modulus in nanocrystalline
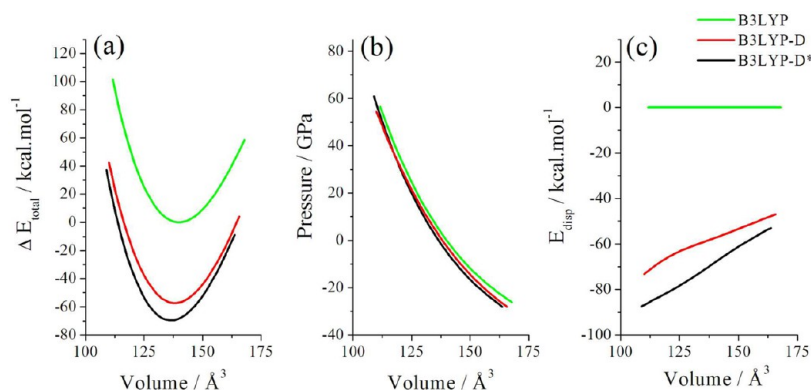
Figure 3. (a) Total energy versus unit cell volume, (b) volume-pressure diagram, and (c) dependence of dispersion energy within volume at B3LYP, B3LYP-D, and B3LYP-D* levels.

Table 2. Bulk Modulus B_0, Bulk Modulus Pressure First Derivative B_0', and Equilibrium Volume V_0 of Anatase Conventional Unit Cell from EOS at B3LYP, B3LYP-D, and B3LYP-D*

method	EOS		
	B_0/GPa	B_0'	V_0/Å^3
B3LYP-D*[a]	206.6	3.07	136.5
B3LYP-D[a]	192.4	2.27	138.1
B3LYP[a]	191.6	2.81	140.0
B3LYP[9]	200.3	2.54	141.3
LDA[63]	175		135.4
GGA[49]	169.9	2.27	141.1
single crystal (s.c.)[47]	179 ± 2	4.5 ± 10	136.3
s.c. (20 nm)[48]	169 ± 9		136.6
s.c. (40 nm)[48]	198 ± 10		136.2
polycrystalline[47]	190 ± 10	5.3 ± 10	

[a]This work and ref 30.

anatase under hydrostatic conditions (up to ∼11 GPa) is strongly dependent on particle size in the range between 20 and 40 nm.[48] Theoretical calculations from GGA (B_0 = 169.9 GPa[49]) and B3LYP (B_0 = 200.3 GPa[9]) have shown a wide range for this property.

Some improvements in the bulk modulus value can be reliable for the thermodynamic assessment of the phase stability and other pressure-related properties.

3.3. Hydrostatic and Uniaxial Pressure. The behaviors of lattice parameters under hydrostatic and uniaxial pressure are shown in Figure 4a−c.

As already stated, the hydrostatic pressure affects all cell parameters at the same time with different intensity due to the softness presented in some directions. In anatase, the [001] direction is more soft than [100] = [010], which explains the higher compressibility in this direction, especially when the uniaxial pressure was applied, due to the tension on a (Figure 4a) and b (Figure 4b) parameters.

The variation of internal coordinate u with external pressure is shown in Figure 4c. The direct relationship of u within d_{Ti-O}^{ap} leads to octahedra distortion (faster in uniaxial than in hydrostatic) due to the tendency of local point-group change from D_{2d} to D_{4d}. It was also observed that while d_{Ti-O}^{eq} decreased under hydrostatic pressure, it tended to increase under the uniaxial due to the tension in [100] and [010] directions.

In both (hydrostatic and uniaxial) strain, for c and u parameters at lower pressures, B3LYP-D had a similar behavior to B3LYP; however at higher pressures, B3LYP-D lattice parameters converged to B3LYP-D* as a consequence of the ratio ($R_{ij,g}/R_{vdW}$) decrease in dumping function. For the a parameter, B3LYP and B3LYP-D* had the same trends under lower pressures because those two frameworks had a better description of this parameter when compared with B3LYP-D for the undistorted structure. (See Table 1.)
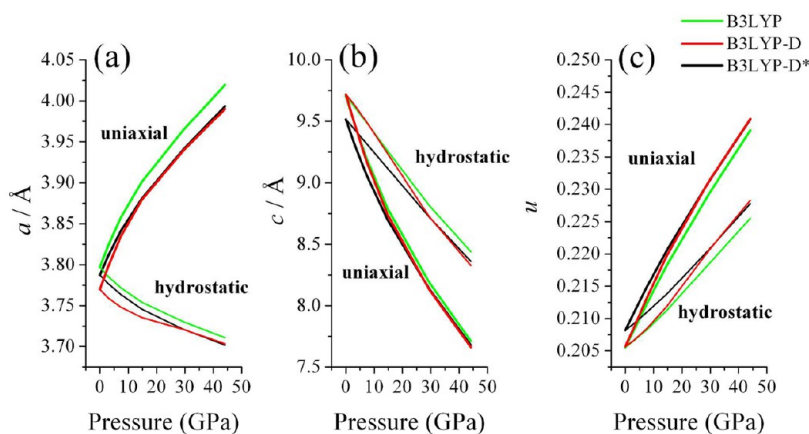
Figure 4. Lattice parameters behavior under hydrostatic and uniaxial strain calculated at B3LYP, B3LYP-D, and B3LYP-D* levels: (a) a parameter, (b) c parameter, and (c) u parameter.

Table 3. Theoretical Elastic Constants C_{ij} (in GPa) of Undistorted and Distorted TiO$_2$ Anatase Bulk at B3LYP-D* Level

	undistorted	hydrostatic/GPa					uniaxial/GPa				
		2.9	7.4	14.7	29.4	44.1	2.9	7.4	14.7	29.4	44.1
C_{11}	319.3	419.3	461.1	530.6	672.9	817.6	401.5	415.7	432.0	444.5	429.2
C_{12}	155.5	159.3	163.4	171.5	182.2	184.3	149.8	141.9	129.7	112.8	103.2
C_{13}	147.0	152.6	158.2	165.0	164.3	153.3	140.4	130.9	115.8	103.0	108.7
C_{33}	233.7	239.1	244.4	251.7	263.0	292.1	236.1	244.4	260.7	300.6	334.9
C_{44}	46.3	44.9	42.9	38.5	18.5	14.2	45.4	37.2	13.6	47.1	128.6
C_{66}	65.9	67.7	70.1	74.3	83.2	91.3	67.7	69.9	72.5	72.8	68.2
B_0[a]	198.5	206.6	213.5	224.2	236.1	252.5	196.5	195.1	193.0	196.0	201.6

[a]Obtained from elastic deformations.

The existence of hydrostatic or uniaxial strain led to different behavior in the bulk elastic constants, as shown in Table 3 calculated at the B3LYP-D* level. Bulk modulus was also determined by the ELASTCON algorithm,[33] where crystalline deformations are followed by geometry optimization and the elastic constants are numerically computed by a Levenberg–Marquardt (LM) curve fitting.[50]

The elastic constants tended to increase within strain in the same direction of C_{ij}, as observed for hydrostatic distorted bulk for C_{11}, C_{12}, C_{13}, C_{33}, and C_{66}. The sharpest C_{ij} increase occurs under hydrostatic pressure for the C_{11} constant, and for C_{33} it occurs under uniaxial pressure due to the expansion of a and b parameters when the pressure was applied only in c.

Under hydrostatic pressure, the C_{13} and C_{44} constants decrease inversely with pressure, even with the reduction of the cell parameters. One must keep in mind that with the shortening of bonds the electronic repulsion increases, and thus the decrease in those constants is related to the atomic repulsion. Furthermore, the C_{44} shear stress is facilitated because it leads to a tension of unit cell.

An only decrease trend was observed for C_{12} and C_{13} under uniaxial pressure due to the expansion of a and b, which also deeply influenced C_{11}. For C_{44}, the behavior under uniaxial strain was very different from hydrostatic, which can be attributed to changing the c/a ratio of 2.51 from undistorted bulk to ≤2 in [001] compressed structure when the pressure was ≥29.4 GPa, thus increasing C_{44} value.

Bulk modulus increased almost linearly under hydrostatic pressure, whereas from uniaxial the B_0 initially decreased (lower than default structure) until 14.7 GPa and subsequently increased. This occurs due to the softness of c and expansion of a and b parameters. Only under pressure >29.4 GPa was the compressed bulk modulus higher than B_0.

The resistance to compression in some directions can be understood by means of charge density maps analysis. In Figure 5, the charge density contour is shown for the (010) plane of anatase conventional cell at B3LYP-D*.

The charge-density distribution at Ti and O sites on the (010) plane (Figure 5) shows that the highest charge density resides in the immediate vicinity of the nuclei with spherical distribution. In the interatomic space, a nonspherical charge distribution indicates the covalent character of Ti−O bond.

At 44.1 GPa, the unit cell under hydrostatic pressure had a variation on apical (d_{Ti-O}^{ap}) and equatorial (d_{Ti-O}^{eq}) Ti−O bond lengths of −7.60 and +7.52 pm, respectively, while under uniaxial pressure an increase in d_{Ti-O}^{eq} of 6.27 pm and a notable decrease in d_{Ti-O}^{ap} of 13.20 pm were observed. As an effect, isolines showed an enhancement on lateral repulsion of Ti centers as compressed under hydrostatic pressure, in which a remarkable increase in C_{11} elastic constant was observed. This
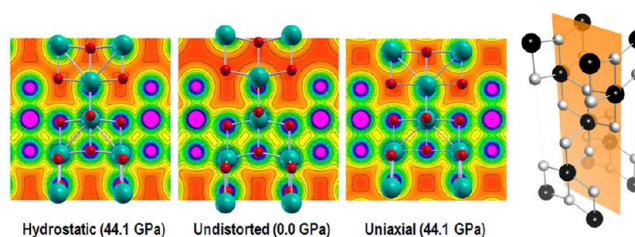

Figure 5. Charge density maps in the (010) plane of conventional unit cell by B3LYP-D* for undistorted and distorted anatase (44.1 GPa). Titanium and oxygen atoms are in green and red spheres, respectively.

effect was mitigated when the system enabled a tension in [100] and [010] directions as a response to external [001] uniaxial pressure, resulting in a more linear chain of O_{eq}−Ti−O_{eq} with an angle 2θ of 175.9 versus 168.5° for the hydrostatic system.

The overlap population analysis showed a relative variation of +10% for Ti−O_{eq} and −47% for Ti−O_{ap} under uniaxial condition as a result of quasilinear O_{eq}−Ti−O_{eq} covalent chain and an inversion on bond length of Ti−O_{ap} > Ti−O_{eq} from undistorted bulk to Ti−O_{eq} > Ti−O_{ap} at ~7 GPa, which led to an ionic repulsion in [001] direction.

For hydrostatic system, the ionic character increased within pressure in all directions. The relative overlap population had a variation of −25% for Ti−O_{eq} and −48% for Ti−O_{ap} at the extreme case of 44.1 GPa.

The {001} family plane has attracted some attention due its lower thermodynamic stability and high reactivity in catalysis and photocatalysis.[8,51−54] Electronic information of (001) plane section in bulk can be extracted from charge density analysis, shown in Figure 6.

The isolines showed a charge density accumulation in oxygen centers (Mulliken charge = −0.9167 |e|, instead −0.8770 |e| in undistorted bulk) and the relative oxidation of titanium (Mulliken charge of +1.84 |e|, instead +1.76 |e| at zero
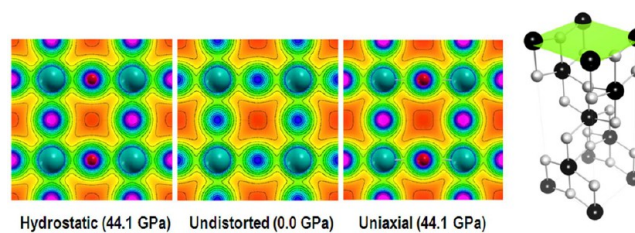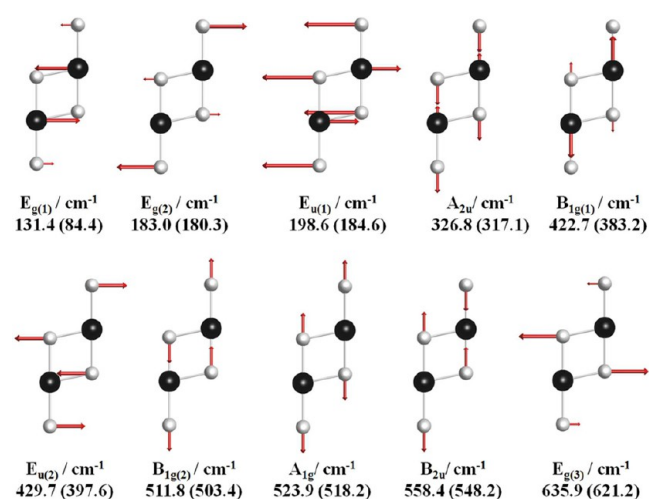

Figure 6. Charge density maps in the (001) plane of conventional unit cell by B3LYP-D* for undistorted and distorted anatase (44.1 GPa). Titanium center are in green spheres and oxygen is in red.

pressure) that led to a higher interatomic repulsion on the (001) plane for hydrostatically compressed unit cell. The pressure in the c axis from uniaxial pressure led to a small variation of Mulliken charges but with inverse behavior in relation to hydrostatic pressure.

Hereinafter, only B3LYP and B3LYP-D* were used for vibrational, electronic band structure, and density of state calculations for distorted structures.

3.4. Vibrational Properties. From the group theory, the tetragonal anatase structure (space group D_{4h}^{19}) has three acoustic modes and 15 optical modes $(A_{1g} + 1A_{2u} + 2B_{1g} + 1B_{2u} + 3E_g + 2E_u)$, in which the terms with subscript u and g are infrared (IR) and Raman (R) active, respectively. The B_{2u} mode is silent. The analysis of IR and R vibrational modes within the pressure enabled evaluates the short-range interactions and the bond behavior under unit cell deformation.

The symmetry of these modes and the predicted frequencies for anatase by B3LYP and B3LYP-D* are shown in Figure 7.

$E_{g(1)}$ / cm^{-1}
131.4 (84.4)

$E_{g(2)}$ / cm^{-1}
183.0 (180.3)

$E_{u(1)}$ / cm^{-1}
198.6 (184.6)

A_{2u} / cm^{-1}
326.8 (317.1)

$B_{1g(1)}$ / cm^{-1}
422.7 (383.2)

$E_{u(2)}$ / cm^{-1}
429.7 (397.6)

$B_{1g(2)}$ / cm^{-1}
511.8 (503.4)

A_{1g} / cm^{-1}
523.9 (518.2)

B_{2u} / cm^{-1}
558.4 (548.2)

$E_{g(3)}$ / cm^{-1}
635.9 (621.2)

Figure 7. Vibrational modes of anatase within frequencies calculated at B3LYP-D* and B3LYP (in parentheses) level. The vectors are on relative and qualitative scales.

The A_{2u} mode is IR-active for light polarized parallel to the [001] direction, and the E_u modes are active for light polarized perpendicular to the c axis. All E_g and E_u modes occur in the [100] and [010] directions and are double-degenerated as a consequence of tetragonal structure (lattice parameters $a = b$).

The A and B modes are in the [001] direction and stretch longitudinally the $Ti-O_{eq}$ bond. The silent mode B_{2u} does not change the dipolar moment and thus is inactive by conventional analysis at the Γ point.

For undistorted structure, vibrational frequencies by B3LYP-D* are in closest agreement with experimental single crystal data than conventional B3LYP. Experimentally, infrared and Raman modes are usually observed at 143 ($E_{g(1)}$), 198 ($E_{g(2)}$), 262 ($E_{u(1)}$), 367 (A_{2u}), 395 ($B_{1g(1)}$), 435 ($E_{u(2)}$), 512 ($B_{1g(2)}$), 518 (A_{1g}), and 639 cm^{-1} ($E_{g(3)}$).[55,56]

The frequency shifts for hydrostatic and uniaxial distorted bulk are shown in Figure 8a,b, respectively.

Calculated B3LYP and B3LYP-D* modes shared the same trends, but the B3LYP modes were more irregular than those of B3LYP-D*. This is particularly true for the modes $E_{g(1)}$ under hydrostatic pressure and $E_{g(1)}$ and $E_{u(1)}$ under uniaxial pressure
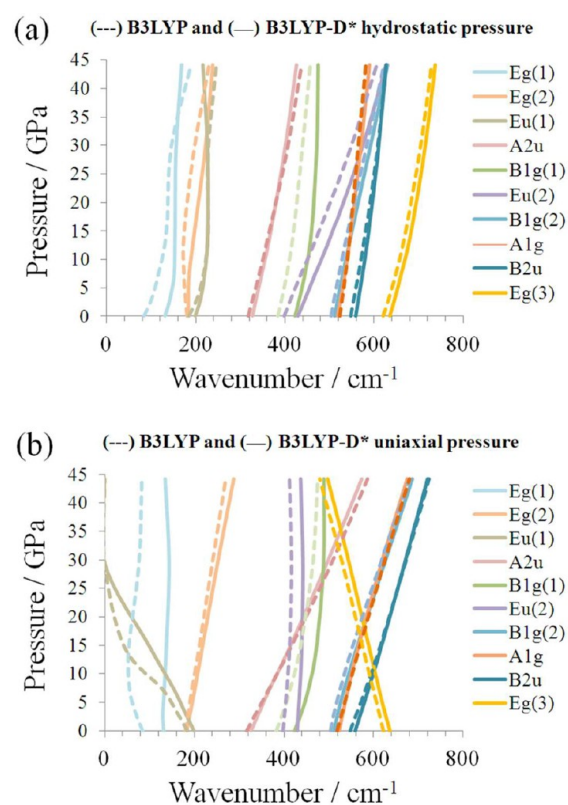
Figure 8. Band shift of vibrational frequencies as a function of (a) hydrostatic and (b) uniaxial pressure calculated by B3LYP and B3LYP-D* methods.

due to the poorer structural description of the B3LYP without the dispersion at higher pressures.

Under hydrostatic pressure, all modes had a blue shift compared with the undistorted anatase, as expected, because under the related strain both Ti–O (apical and equatorial) bonds tended to decrease monotonically, thus increasing the energy need to vibrate: $[\partial(v_i - v_{\text{default}})/\partial P]_T > 0$. However, an odd behavior was observed for the mode $E_{u(1)}$, which above 14.7 GPa had a red shift when compared with the previous compressed structure $[\partial(v_i - v_{i-1})/\partial P]_T$. It can be explained by correlating the vibrational modes within elastic constants (Table 3) because of the intrinsic relationship of vibration vector mode and symmetry. The odd behavior of the $E_{u(1)}$ mode can be attributed to vectors that are in same direction as C_{13} and C_{44}, that decreased above 14.7 GPa, as shown in Table 3.

Under uniaxial pressure, most modes have a blue shift relative to undistorted structure, but all two-dimensional E modes had odd behavior, except the $E_{g(2)}$, because under uniaxial compression the expansion of a and b is allowed by the full-relaxed optimization procedure; thus, while the apical Ti–O bond decreased, the equatorial increased. The modes $E_{u(1)}$ and $E_{g(3)}$ presented a red shift when compared with the undistorted one. This happened because they are very dependent on the equatorial bonds; besides the constants C_{12} and C_{13} were softened under the pressure. The $E_{g(1)}$ had a sequence of red shift (compared with the undistorted structure) → blue shift → red shift (compared with the last compressed structure) by the same explanation as the red shift behavior for $E_{g(3)}$. The difference between those two modes is that the principal vectors in $E_{g(3)}$ are in lighter atom (O), whereas for

Table 4. Band Gap (eV) at High Symmetric *k* Points in the First Brillouin Zone[a]

method	path	Γ	X	Σ	Z	Σ_1	N	P
B3LYP	direct	**3.91**	4.87	5.81	3.98	4.97	5.51	5.29
	indirect		3.61	4.38	**3.60**	4.15	4.23	3.81
B3LYP-D	direct	**3.96**	4.91	5.91	4.02	5.03	5.61	5.35
	indirect		3.64	4.44	**3.64**	4.20	4.29	3.83
B3LYP-D*	direct	**3.94**	4.97	5.92	4.03	5.03	5.54	5.41
	indirect		**3.55**	4.45	3.61	4.18	4.20	3.75

[a]Bold-faced attached the lower direct ($\Gamma \rightarrow \Gamma$) and indirect ($k$ point $\rightarrow \Gamma$) band gaps.
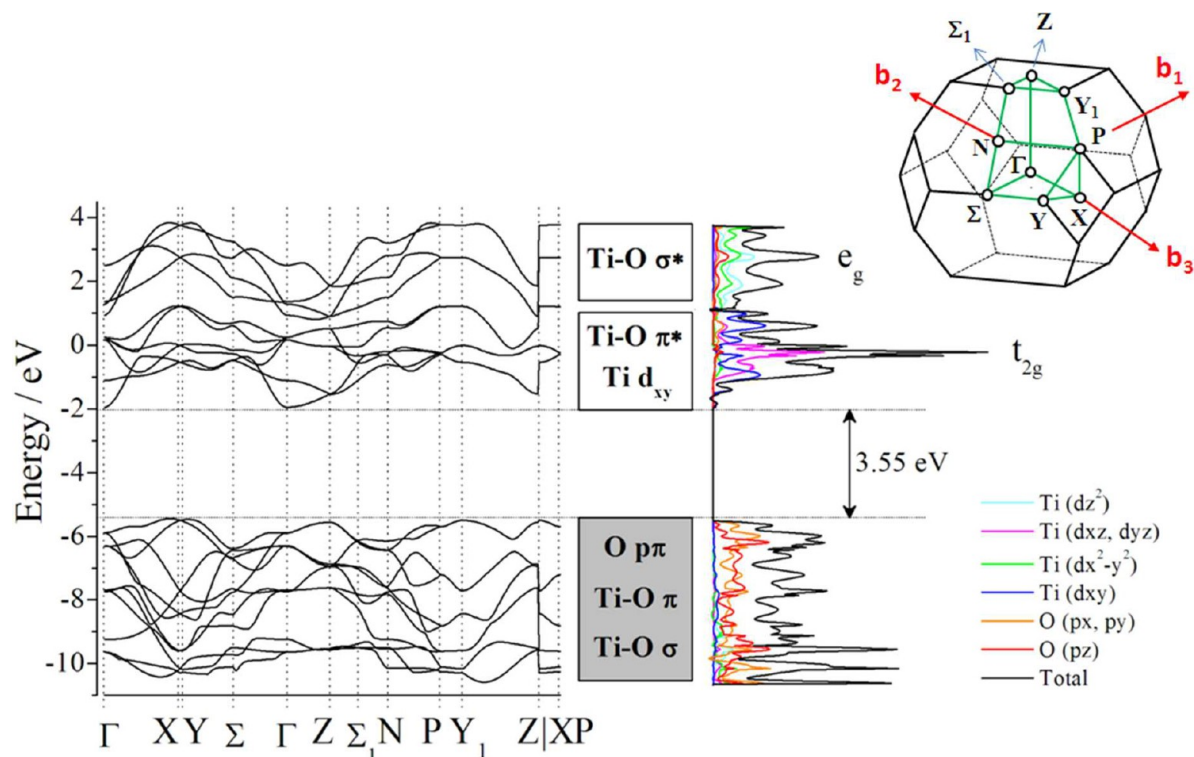

Figure 9. Band structure and projected density of states (PDOS) for undistorted anatase at B3LYP-D* level. The inset shows the Brillouin zone.

$E_{g(1)}$ they are in the heavier centers (Ti). The only blue-shift behavior observed for a 2-D mode was for $E_{g(2)}$ because the principal vector of this mode is in apical position, where Ti−O_{ap} decreases with wavenumber increase.

Sekiya et al.[57] investigated the influence of pressure up to 6.7 GPa applied to anatase TiO_2 by Raman spectroscopy and observed that frequencies changed linearly within the pressure and most modes had a blue shift. However, they also observed that $E_{g(2)}$ frequencies decreased under hydrostatic pressure and stated that this mode played an important role in the pressure-induced phase transition (that occurred at 4.3 GPa). The behavior of $E_{g(2)}$ was also previously reported by Ohsaka et al.[58] without linear decrease. This behavior was also observed in the present study.

3.5. Electronic Structure. The role of dispersion energy on the band structures was also examined, and the calculated direct (d) and indirect (id) band gaps at high symmetric k points are displayed in Table 4.

The smallest direct band gap was found for $\Gamma \rightarrow \Gamma$ point at all levels. The smallest indirect band gap changed its path with the inclusion of dispersion energy as a consequence of structural improvement. The absolute values of calculated band gaps for anatase by B3LYP-D* (3.94[(d)] and 3.55[(id)] eV)

were in close agreement with experimental ones (3.53[(d)] and 3.20[(id)] eV)[59] and recent computations using HSE06 hybrid functional (3.60[(id)] eV).[60] Although B3LYP-D* had overestimated the band gap of TiO_2, the general trends should not be neglected.

In relation to B3LYP, the shift of band gap energies on B3LYP-D* resulted from structural improvement by the dispersion inclusion, with the shortening of Ti−O bonds and adjustment of crystal-lattice parameters.

Figure 9 shows the electronic band structure and density of states (DOS) for undistorted anatase at the B3LYP-D* level. The band structure was constructed along the high-symmetry direction of the first Brillouin zone.

The DOS analysis of TiO_2 anatase (Figure 9) showed that the valence band (VB) is composed mostly of oxygen, and the conduction band (CB) is composed mostly of titanium. A good qualitative description for anatase electronic structure can be found in ref 61. From PDOS analysis, Ti centers contributed to CB with e_g (d_z^2 and $d_{x^2-y^2}$) and t_{2g} (d_{xy}, d_{xz}, and d_{yz}) orbitals, while oxygen contributed to p_x, p_y, and p_z orbitals.

From the viewpoint of chemical bond, orbital overlap regions in PDOS allowed us to build the diagram shown in Figure 9, where at lower energies Ti−O σ bonds are formed by overlap

of O (p_z and $p_x p_y$) and Ti (d_z^2 and $d_{x^2-y^2}$) orbitals in the Ti_3O cluster plane; Ti−O π bonds out of the Ti_3O cluster plane are in the middle energy of VB; and at the top of the VB we observed the O ($p\pi$) nonbonding states. In CB, Ti (3d) splitting can be explained by the crystal field theory in the octahedra field, where the bottom is composed mainly of Ti (d_{xy}) and Ti−O π^* (d_{xz}, d_{yz}) states in the t_{2g} region and at high energies by Ti−O σ^* (d_z^2, $d_{x^2-y^2}$) bonds in the e_g states. Degenerated states emerged from tetragonal symmetry.

The external pressure effect over electronic band gap path at the B3LYP-D* is shown in Figure 10.
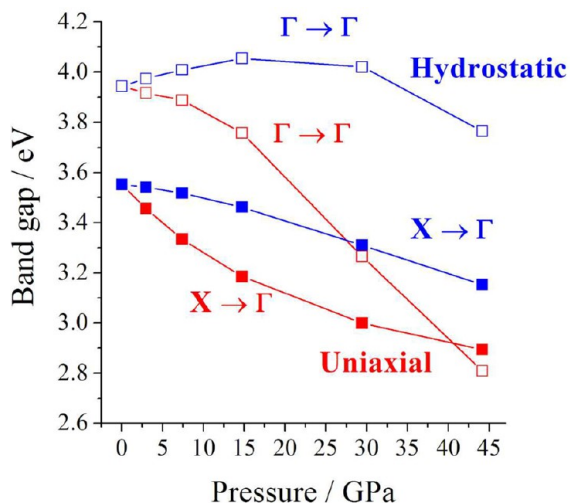
Figure 10. Behavior of direct and indirect band gap under hydrostatic and uniaxial pressure at B3LYP-D* level.

Hydrostatic and uniaxial strain had different effects on the band gap path and its absolute values. Under the adopted pressure range, the indirect (X → Γ) band gap always decreased with pressure and is lower than the direct (Γ → Γ) one for hydrostatic, which increased up to 15 GPa and decreased after this pressure. For the strained unit cell in the [001] direction, a crossing point of direct and indirect band gap at ~40 GPa was observed, above which anatase became a direct semiconductor with gap of ~2.8 eV. Although the anatase phase is not thermodynamically stable at these pressures, insights using this model can be useful for local strain with this structure.

The elucidation of band gap behavior within pressure can be found by means of PDOS analysis, as shown in Figure 11.

Under hydrostatic pressure, Figure 11a, the top of VB and the bottom of CB increased within pressure, with a major impact on VB as a result of bond length decrease and the increase in bond energy. The tendency of increasing the local [TiO_6] octahedra symmetry (from D_{2h} to O_h), led to a degeneration of O ($p_x p_y$) with O (p_z) and Ti (d_{xz}, d_{yz}) with Ti (d_{xy}) orbitals. A significant change in the shape of PDOS above 14.7 GPa was also observed.

The top of VB increased (~0.5 eV, from 0.0 to 44.1 GPa), and the bottom of CB decreased slowly under uniaxial strain (Figure 11b), unlike the hydrostatic one (Figure 11a). The global effect on total DOS for uniaxial pressure came from the Ti−O_{ap} decrease and Ti−O_{eq} increase with pressure. The energy states response followed the anisotropy and directionality of external pressure. At high pressures, a split in Ti e_g crystalline orbitals followed the predicted order of octahedra

D_{4d} for Ti−O_{ap} < Ti−O_{eq}, which is, in ascending order: d_{xy} > (d_{xz} = d_{yz}) > $d_{x^2-y^2}$ > d_z^2.

3.6. Model System for Octahedra Distortion. The PDOS for idealized high-symmetry anatase unit cell were also studied (Figure 12). These structures were: (i) extended Ti−O apical bond (planar square-like, D_{4d}) with default lattice parameters (a_0, c_0) from undistorted bulk and the extreme value of u = 0.250; (ii) perfect octahedra [TiO_6] (O_h local symmetry) with lattice parameters {a_0, $c = 2a_0$, u = 0.250}; and (iii) {$a = c_0/2$, c_0, u = 0.250}.

The PDOS for D_{4d} structure presented the edge of VB composed mainly of O $p\pi$ nonbonding orbital and deep states composed of Ti−O σ bond by the $d_{x^2-y^2}$ and $p_x p_y$ overlap. At the middle energies, the VB was composed mainly of Ti−O π bonding states. The orbital splitting due to [TiO_6] distortion was observed in CB, where the apical Ti−O increase led to a planar square structure, with the ascending order of t_{2g} and e_g orbitals: (d_{xz} = d_{yz}) > d_{xy} ≈ d_z^2 > $d_{x^2-y^2}$ and massive contribution of antibonding p_z oxygen orbital.

For periodic unit cells with local [TiO_6] O_h symmetry, PDOS clearly showed a degeneration for Ti t_{2g} and e_g orbitals. The O ($p_x p_y p_z$) became nonhybridized-like orbitals and fully occupied its respective axis. The lattice parameters changed between {a_0, $c = 2a_0$, u = 0.250} and {$a = c_0/2$, c_0, u = 0.250}, in relation to default ones that modified the absolute energies of states but conserved the symmetry and profile of PDOS, as shown in Figure 12.

4. CONCLUSIONS

The lattice parameter improvements with the inclusion of adjusted Grimme dispersion (B3LYP-D*) for TiO_2 with anatase structure led to a more stable structure under zero external pressure conditions when compared with B3LYP and B3LYP-D (from EOS results).

The structural improvement by B3LYP-D* allowed us to investigate anatase structure at high pressures with reliable description by means of hydrostatic and [001] uniaxial pressure in the range of 0.0 to 44 GPa. Also, it was observed at higher pressures that B3LYP-D and B3LYP-D* shared structural similarities.

The behavior of elastic constants with pressure allowed us to describe the soft directions in the bulk. The overall constants and bulk modulus increased under hydrostatic pressure. Under uniaxial pressure, the tension in [100] and [010] directions led to an increase in equatorial Ti−O bonds and decreased the apical one, which led to fluctuation in elastic constants behavior and B_0.

The vibrational modes at Γ point were evaluated, and its behavior within pressure was discussed based on the symmetry of the modes, related elastic constants, and direction of external pressure. A blue shift was observed for overall hydrostatically compressed structures, whereas for the c-compressed structure a red shift was observed for the 2-D modes. Furthermore, the red shift behavior of Raman $E_{g(2)}$ mode up to ~4 GPa already observed by experimentalists under hydrostatic pressure was also observed under B3LYP-D* in this study.

The changes of indirect band gap path were observed with the inclusion of dispersion. For B3LYP-D*, a decrease in band gap with pressure was observed. Under uniaxial pressure, a notable change occurred at ~40 GPa, in which anatase became a direct semiconductor with band gap ~2.8 eV.

The role of local [TiO_6] symmetry changing D_{2h} → D_{4h} → O_h was investigated by means of PDOS, and the degeneracy of

7058

dx.doi.org/10.1021/jp311572y | *J. Phys. Chem. C* 2013, 117, 7050−7061
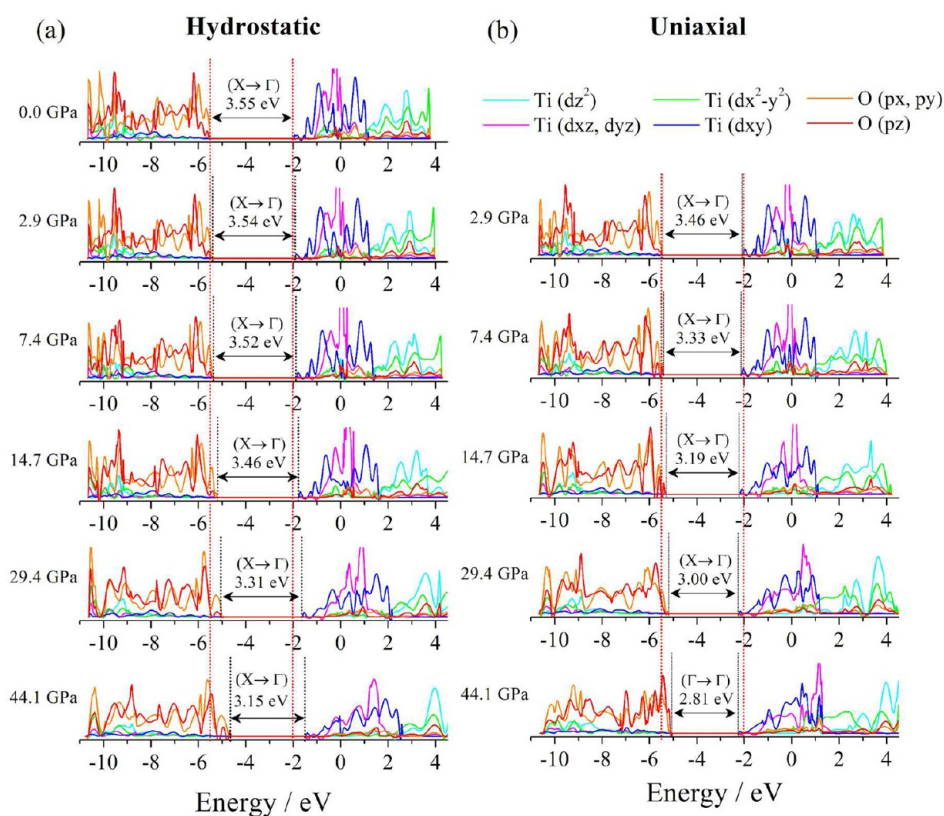
Figure 11. Projected density of states (PDOS) of TiO_2 anatase under (a) hydrostatic and (b) uniaxial pressure at B3LYP-D*. Vertical red line shows the top of VB and bottom of CB for undistorted structure.
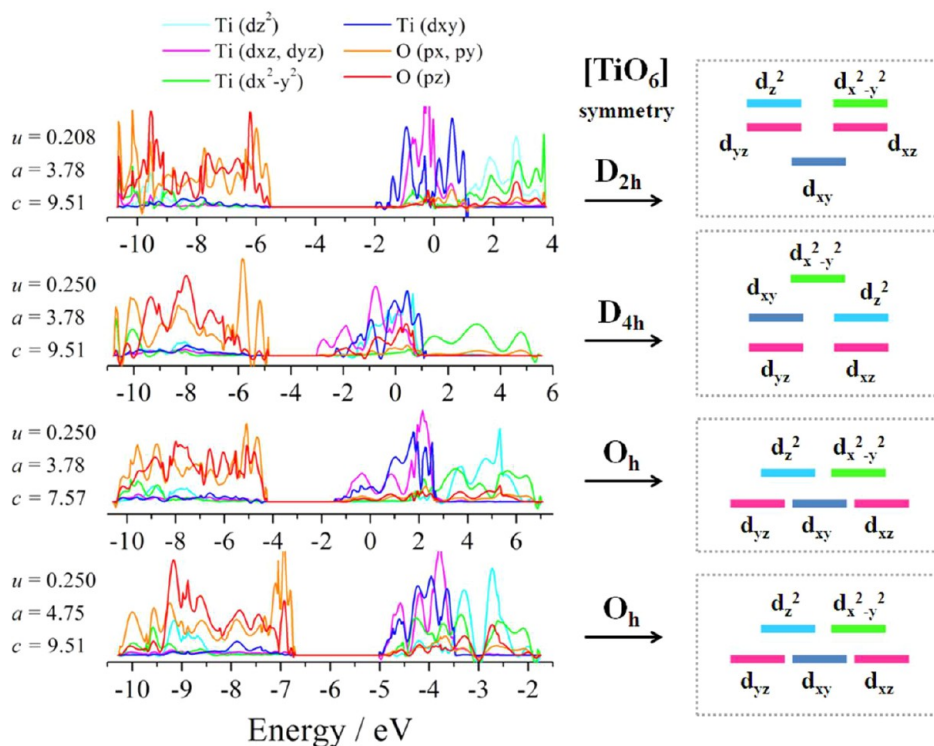
Figure 12. Projected density of states (PDOS) of TiO_2 anatase under different local octahedra symmetry from $D_{2d} \rightarrow D_{4d} \rightarrow O_h$ at the B3LYP-D* level.

some states was observed. Some insights about these idealized structures are fruitful for local effects by dopants and other structural modifiers in anatase bulk.

Investigations involving photoluminescence phenomena due to $[TiO_6]_o - [TiO_6]_d$ cluster interaction are already in development in our group, whereas the chemical potential of point

defects within pressure and the introduction of electronic levels into forbidden band gap are also explored.

■ ASSOCIATED CONTENT

Ⓢ Supporting Information

Tables show calculated lattice parameters, Ti—O length and angles, band gap energies, vibrational frequencies, and Mulliken population analysis, for all structures under uniaxial and hydrostatic pressure using B3LYP, B3LYP-D, and B3LYP-D*. This material is available free of charge via the Internet at http://pubs.acs.org.

■ AUTHOR INFORMATION

Corresponding Author
*Tel: +55 14 313066096. Fax: +55 14 313066096. E-mail: sambrano@fc.unesp.br.

Notes

The authors declare no competing financial interest.

■ ACKNOWLEDGMENTS

■ REFERENCES

(1) Fujishima, A.; Honda, K. Electrochemical Photolysis of Water at a Semiconductor Electrode. *Nature* **1972**, *238*, 37−38.

(2) Oregan, B.; Gratzel, M. A Low-Cost, High-Efficiency Solar-Cell Based on Dye-Sensitized Colloidal TiO_2 Films. *Nature* **1991**, *353*, 737−740.

(3) Bak, T.; Nowotny, J.; Sucher, N. J.; Wachsman, E. Effect of Crystal Imperfections on Reactivity and Photoreactivity of TiO_2 (Rutile) with Oxygen, Water, and Bacteria. *J. Phys. Chem. C.* **2011**, *115*, 15711−15738.

(4) Bruix, A.; Rodriguez, J. A.; Ramirez, P. J.; Senanayake, S. D.; Evans, J.; Park, J. B.; Stacchiola, D.; Liu, P.; Hrbek, J.; Illas, F. A New Type of Strong Metal-Support Interaction and the Production of H_2 Through the Transformation of Water on $Pt/CeO_2(111)$ and $Pt/CeO_x/TiO_2(110)$ Catalysts. *J. Am. Chem. Soc.* **2012**, *134*, 8968−8974.

(5) Diebold, U. The Surface Science of Titanium Dioxide. *Surf. Sci. Rep.* **2003**, *48*, 53−229.

(6) Evarestov, R. A.; Bandura, A. B.; Losev, M. V. Symmetry and Stability of Nanotubes Based on Titanium Dioxide. *Russ. J. Gen. Chem.* **2010**, *80*, 1152−1167.

(7) Ichimura, A. S.; Mack, B. M.; Usmani, S. M.; Mars, D. G. Direct Synthesis of Anatase Films with Similar to 100% (001) Facets and [001] Preferred Orientation. *Chem. Mater.* **2012**, *24*, 2324−2329.

(8) Yang, H. G.; Sun, C. H.; Qiao, S. Z.; Zou, J.; Liu, G.; Smith, S. C.; Cheng, H. M.; Lu, G. Q. Anatase TiO_2 Single Crystals With a Large Percentage of Reactive Facets. *Nature* **2008**, *453*, 638−641.

(9) Calatayud, M.; Mori-Sanchez, P.; Beltran, A.; Pendas, A. M.; Francisco, E.; Andres, J.; Recio, J. M. Quantum-Mechanical Analysis of the Equation of State of Anatase TiO_2. *Phys. Rev. B* **2001**, *64*, 184113-1−184113-9.

(10) Abbasnejad, M.; Shojaee, E.; Mohammadizadeh, M. R.; Alaei, M.; Maezono, R. Quantum Monte Carlo Study of High-Pressure Cubic TiO_2. *Appl. Phys. Lett.* **2012**, *100*, 261902-1−261902-4.

(11) Bapna, K.; Choudhary, R. J.; Phase, D. M. Evolution of Different Structural Phases of TiO_2 Films With Oxygen Partial Pressure and Fe Doping and Their Electrical Properties. *Mater. Res. Bull.* **2012**, *47*, 2001−2007.

(12) Escudero, A.; Langenhorst, F. Chromium Incorporation Into TiO_2 at High Pressure. *J. Solid State. Chem.* **2012**, *190*, 61−67.

(13) Escudero, A.; Langenhorst, F. Incorporation of Si Into TiO_2 Phases at High Pressure. *Am. Mineral.* **2012**, *97*, 524−531.

(14) Escudero, A.; Langenhorst, F.; Muller, W. F. Aluminum Solubility in TiO_2 Rutile at High Pressure and Experimental Evidence for a $CaCl_2$-Structured Polymorph. *Am. Mineral.* **2012**, *97*, 1075−1082.

(15) Mahmood, T.; Cao, C. B.; Khan, W. S.; Usman, Z.; Butt, F. K.; Hussain, S. Electronic, Elastic, Optical Properties of Rutile TiO_2 Under Pressure: A DFT Study. *Physica B.* **2012**, *407*, 958−965.

(16) Yoo, D. S.; Ahn, K.; Cho, S. B.; Lee, M.; Chung, Y. C. Oxygen Vacancy Chain Formation in TiO_2 Under External Strain for Resistive Switching Memory. *Jpn. J. Appl. Phys.* **2012**, *51*, 4.

(17) Yang, B.; Liu, F.; Lagally, M. G. Local Strain-Mediated Chemical Potential Control of Quantum Dot Self-Organization in Hetero-epitaxy. *Phys. Rev. Lett.* **2004**, *92*, 025502-1−025502-4.

(18) Beltran, A.; Gracia, L.; Andres, J. Density Functional Theory Study of the Brookite Surfaces and Phase Transitions Between Natural Titania Polymorphs. *J. Phys. Chem. B.* **2006**, *110*, 23417−23423.

(19) Thulin, L.; Guerra, J. Calculations of Strain-Modified Anatase TiO_2 Band Structures. *Phys. Rev. B.* **2008**, *77*, 195112−5.

(20) Yin, W.-J.; Chen, S.; Yang, J.-H.; Gong, X.-G.; Yan, Y.; Wei, S.-H. Effective Band Gap Narrowing of Anatase TiO_2 by Strain Along a Soft Crystal Direction. *Appl. Phys. Lett.* **2010**, *96*, 221901-1−221901-3.

(21) Civalleri, B.; Maschio, L.; Ugliengo, P.; Zicovich-Wilson, C. M. Role of Dispersive Interactions in the CO Adsorption on MgO(001): Periodic B3LYP Calculations Augmented with an Empirical Dispersion Term. *Phys. Chem. Chem. Phys.* **2010**, *12*, 6382−6386.

(22) Civalleri, B.; Zicovich-Wilson, C. M.; Valenzano, L.; Ugliengo, P. B3LYP Augmented with an Empirical Dispersion Term (B3LYP-D*) as Applied to Molecular Crystals. *CrystEngComm.* **2008**, *10*, 405−410.

(23) Civalleri, B.; Zicovich-Wilson, C. M.; Valenzano, L.; Ugliengo, P. B3LYP Augmented with an Empirical Dispersion Term (B3LYP-D*) as Applied to Molecular Crystals. *CrystEngComm.* **2008**, *10*, 1693−1693.

(24) Parac, M.; Etinski, M.; Peric, M.; Grimme, S. A Theoretical Investigation of the Geometries and Binding Energies of Molecular Tweezer and Clip Host-Guest Systems. *J. Chem. Theory Comput.* **2005**, *1*, 1110−1118.

(25) Piacenza, M.; Grimme, S. van der Waals Complexes of Polar Aromatic Molecules: Unexpected Structures for Dimers of Azulene. *J. Am. Chem. Soc.* **2005**, *127*, 14841−14848.

(26) Grimme, S. Semiempirical GGA-Type Density Functional Constructed with a Long-Range Dispersion Correction. *J. Comput. Chem.* **2006**, *27*, 1787−1799.

(27) Dovesi, R.; Saunders, V. R.; Roetti, C.; Orlando, R.; Zicovich-Wilson, C. M.; Pascale, F.; Civalleri, B.; Doll, K.; Harrison, N. M.; Bush, I. J.; et al. *CRYSTAL09 User's Manual*; University of Torino: Torino, Italy, 2009.

(28) Dovesi, R.; Orlando, R.; Civalleri, B.; Roetti, C.; Saunders, V. R.; Zicovich-Wilson, C. M. CRYSTAL: A Computational Tool for the Ab Initio Study of the Electronic Properties of Crystals. *Z. Kristallogr.* **2005**, *220*, 571−573.

(29) Grimme, S. Accurate Description of Van Der Waals Complexes by Density Functional Theory Including Empirical Corrections. *J. Comput. Chem.* **2004**, *25*, 1463−1473.

(30) Albuquerque, A. R; Garzim, M. L; Santos, I. M. G; Longo, V. M.; Longo, E.; Sambrano, J. R. DFT Study with Inclusion of the Grimme Potential on Anatase $TiO2$: Structure, Electronic and Vibrational Analyses. *J. Phys. Chem. A.* **2012**, *116*, 11731−11735.

(31) Becke, A. D. Density-Functional Thermochemistry 3. The Role of Exact Exchange. *J. Chem. Phys.* **1993**, *98*, 5648−5652.

(32) Lee, C. T.; Yang, W. T.; Parr, R. G. Development of the Colle-Salvetti Correlation-Energy Formula into a Functional of the Electron-Density. *Phys. Rev. B.* **1988**, *37*, 785−789.

(33) Perger, W. F.; Criswell, J.; Civalleri, B.; Dovesi, R. Ab-Initio Calculation of Elastic Constants of Crystalline Systems With the CRYSTAL Code. *Comput. Phys. Commun.* **2009**, *180*, 1753−1759.

(34) Birch, F. Finite Elastic Strain of Cubic Crystals. *Phys. Rev.* **1947**, *71*, 809−824.

(35) Zicovich-Wilson, C. M.; Pascale, F.; Roetti, C.; Saunders, V. R.; Orlando, R.; Dovesi, R. Calculation of the Vibration Frequencies of Alpha-Quartz: The Effect of Hamiltonian and Basis Set. *J. Comput. Chem.* **2004**, *25*, 1873−1881.

(36) Pascale, F.; Zicovich-Wilson, C. M.; Gejo, F. L.; Civalleri, B.; Orlando, R.; Dovesi, R. The Calculation of the Vibrational Frequencies of Crystalline Compounds and its Implementation in the CRYSTAL Code. *J. Comput. Chem.* **2004**, *25*, 888−897.

(37) Setyawan, W.; Curtarolo, S. High-Throughput Electronic Band Structure Calculations: Challenges and Tools. *Comput. Mater. Sci.* **2010**, *49*, 299−312.

(38) Ugliengo, P.; Viterbo, D.; Chiari, G. Moldraw - Molecular Graphics on a Personal-Computer. *Z. Kristallogr.* **1993**, *207*, 9−23.

(39) Momma, K.; Izumi, F. VESTA 3 for Three-Dimensional Visualization of Crystal, Volumetric and Morphology Data. *J. Appl. Crystallogr.* **2011**, *44*, 1272−1276.

(40) Kokalj, A. Computer Graphics and Graphical User Interfaces as Tools in Simulations of Matter at the Atomic Scale. *Comput. Mater. Sci.* **2003**, *28*, 155−168.

(41) Vetter Ferri, E. A.; Mazzo, T. M.; Longo, V. M.; Moraes, E.; Pizani, P. S.; Li, M. S.; Martinez Espinosa, J. W.; Varela, J. A.; Longo, E. Very Intense Distinct Blue and Red Photoluminescence Emission in MgTiO3 Thin Films Prepared by the Polymeric Precursor Method: An Experimental and Theoretical Approach. *J. Phys. Chem. C.* **2012**, *116*, 15557−15567.

(42) Longo, V. M.; de Figueiredo, A. T.; Campos, A. B.; Espinosa, J. W. M.; Hernandes, A. C.; Taft, C. A.; Sambrano, J. R.; Varela, J. A.; Longo, E. Different Origins of Green-Light Photoluminescence Emission in Structurally Ordered and Disordered Powders of Calcium Molybdate. *J. Phys. Chem. A.* **2008**, *112*, 8920−8928.

(43) Cavalcante, L. S.; Longo, V. M.; Zampieri, M.; Espinosa, J. W. M.; Pizani, P. S.; Sambrano, J. R.; Varela, J. A.; Longo, E.; Simoes, M. L.; Paskocimas, C. A. Experimental and Theoretical Correlation of Very Intense Visible Green Photoluminescence in BaZrO₃ Powders. *J. Appl. Phys.* **2008**, *103*, 063527-1−063527-8.

(44) Longo, V. M.; Cavalcante, L. S.; Erlo, R.; Mastelaro, V. R.; de Figueiredo, A. T.; Sambrano, J. R.; de Lazaro, S.; Freitas, A. Z.; Gomes, L.; Vieira, N. D., Jr.; et al. Strong Violet-Blue Light Photoluminescence Emission at Room Temperature in SrZrO₃: Joint Experimental and Theoretical Study. *Acta Mater.* **2008**, *56*, 2191−2202.

(45) Deak, P.; Aradi, B.; Frauenheim, T. Polaronic Effects in TiO₂ Calculated by the HSE06 Hybrid Functional: Dopant Passivation by Carrier Self-Trapping. *Phys. Rev. B.* **2011**, *83*, 155207-1−155207-7.

(46) Horn, M.; Schwerdt, Cf; Meagher, E. P. Refinement of Structure of Anatase at Several Temperatures. *Z. Kristallogr.* **1972**, *136*, 273−281.

(47) Arlt, T.; Bermejo, M.; Blanco, M. A.; Gerward, L.; Jiang, J. Z.; Olsen, J. S.; Recio, J. M. High-Pressure Polymorphs of Anatase TiO₂. *Phys. Rev. B.* **2000**, *61*, 14414−14419.

(48) Al-Khatatbeh, Y.; Lee, K. K. M.; Kiefer, B. Compressibility of Nanocrystalline TiO₂ Anatase. *J. Phys. Chem. C.* **2012**, *116*, 21635−21639.

(49) Arroyo-de Dompablo, M. E.; Morales-Garcia, A. Taravillo, M. DFT Plus U Calculations of Crystal Lattice, Electronic Structure, and Phase Stability Under Pressure of TiO₂ Polymorphs. *J. Chem. Phys.* **2011**, *135*, 054503-1−054503-9.

(50) Marquardt, D. W. An Algorithm for Least-Squares Estimation of Nonlinear Parameters. *J. Soc. Ind. Appl. Math.* **1963**, *11*, 431−441.

(51) Chen, C.; Hu, R.; Mai, K. G.; Ren, Z. M.; Wang, H.; Qian, G. D.; Wang, Z. Y. Shape Evolution of Highly Crystalline Anatase TiO₂ Nanobipyramids. *Cryst. Growth. Des.* **2011**, *11*, 5221−5226.

(52) Fang, W. Q.; Zhou, J. Z.; Liu, J.; Chen, Z. G.; Yang, C.; Sun, C. H.; Qian, G. R.; Zou, J.; Qiao, S. Z.; Yang, H. G. Hierarchical Structures of Single-Crystalline Anatase TiO₂ Nanosheets Dominated by {001} Facets. *Chem.—Eur. J.* **2011**, *17*, 1423−1427.

(53) Liu, S. W.; Yu, J. G.; Jaroniec, M. Anatase TiO₂ with Dominant High-Energy {001} Facets: Synthesis, Properties, and Applications. *Chem. Mater.* **2011**, *23*, 4085−4093.

(54) Pan, J.; Liu, G.; Lu, G. M.; Cheng, H. M. On the True Photoreactivity Order of {001}, {010}, and {101} Facets of Anatase TiO₂ Crystals. *Angew. Chem., Int. Ed.* **2011**, *50*, 2133−2137.

(55) Giarola, M.; Sanson, A.; Monti, F.; Mariotto, G.; Bettinelli, M.; Speghini, A.; Salviulo, G. Vibrational Dynamics of Anatase TiO₂: Polarized Raman Spectroscopy and Ab Initio Calculations. *Phys. Rev. B.* **2010**, *81*, 174305-1−174305-7.

(56) Gonzalez, R. J.; Zallen, R.; Berger, H. Infrared Reflectivity and Lattice Fundamentals in Anatase TiO₂. *Phys. Rev. B.* **1997**, *55*, 7014−7017.

(57) Sekiya, T.; Ohta, S.; Kamei, S.; Hanakawa, M.; Kurita, S. Raman Spectroscopy and Phase Transition of Anatase TiO₂ under High Pressure. *J. Phys. Chem. Solids.* **2001**, *62*, 717−721.

(58) Ohsaka, T.; Yamaoka, S.; Shimomura, O. Effect of Hydrostatic-Pressure on The Raman-Spectrum of Anatase (TiO₂). *Solid State Commun.* **1979**, *30*, 345−347.

(59) Reyes-Coronado, D.; Rodriguez-Gattorno, G.; Espinosa-Pesqueira, M. E.; Cab, C.; de Coss, R.; Oskam, G. Phase-Pure TiO₂ Nanoparticles: Anatase, Brookite and Rutile. *Nanotechnology* **2008**, *19*, 145605-1−145605-10.

(60) Landmann, M.; Rauls, E.; Schmidt, W. G. The Electronic Structure and Optical Response of Rutile, Anatase and Brookite TiO₂. *J. Phys.: Condens. Mat.* **2012**, *24*, 195503-1−195503-6.

(61) Asahi, R.; Taga, Y.; Mannstadt, W.; Freeman, A. J. Electronic and Optical Properties of Anatase TiO₂. *Phys. Rev. B* **2000**, *61*, 7459−7465.

(62) Beltran, A.; Sambrano, J. R.; Calatayud, M.; Sensato, F. R.; Andres, J. Static Simulation of Bulk and Selected Surfaces of Anatase TiO₂. *Surf. Sci.* **2001**, *490*, 116−124.

(63) Mei, Z. G.; Wang, Y.; Shang, S. L.; Liu, Z. K. First-Principles Study of Lattice Dynamics and Thermodynamics of TiO₂ Polymorphs. *Inorg. Chem.* **2011**, *50*, 6996−7003.